Supplementary Information (SI) for Journal of Materials Chemistry A.
This journal is © The Royal Society of Chemistry 2024

Electronic Supplementary Information (ESI)

Carbothermal Reduction-Induced Oxygen Vacancy in Spinel Cathode for High-Performance Aqueous Zinc-Ion Battery

Saheb Bag,[a] *Venkata Surya Kumar Choutipalli,*[b] *Abhirup Bhadra,*[c] *Kevin L. Shuford,*[b] *Dipan Kundu,*[c,d] *and C. Retna Raj**[a]

[a]Functional Materials and Electrochemistry Lab, Department of Chemistry Indian Institute of Technology Kharagpur, Kharagpur 721302, India

[b]Department of Chemistry and Biochemistry, Baylor University, One Bear Place #97348, Waco, Texas 76798-7348, United States

[c]School of Chemical Engineering, University of New South Wales, Sydney, Kensington, NSW 2052, Australia

[d]School of Mechanical & Manufacturing Engineering, University of New South Wales, Sydney, Kensington, NSW 2052, Australia

*** Corresponding Author**

E-mail: crraj@chem.iitkgp.ac.in (C. R. Raj)

Scheme S1. Schematic illustration of the synthesis of O_V-ZnV_2O_4.

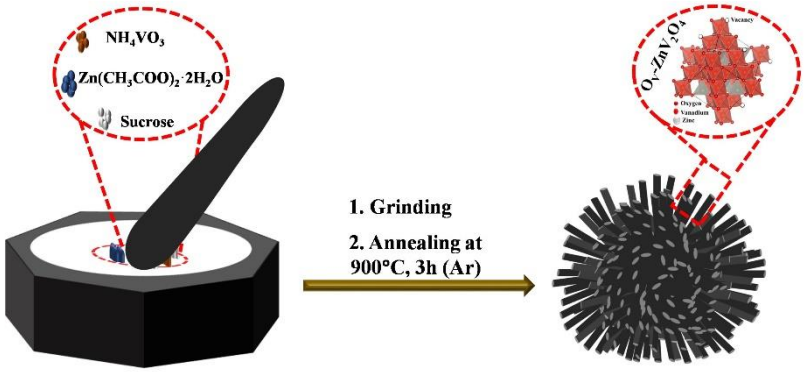

Fig. S1 High-resolution XPS Zn 2p (a), O 1s (b), and C 1s (c) profiles of O_V-ZnV_2O_4-200.

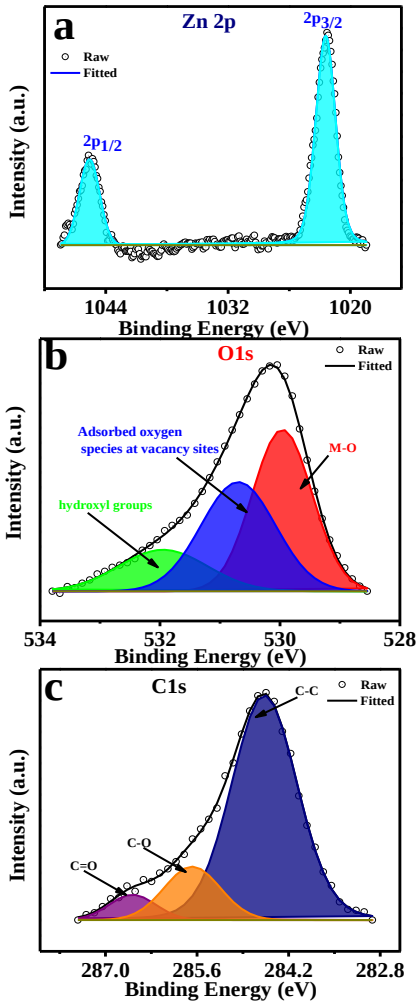

Fig. S2 Thermogravimetric (TG) analyses illustrating the decomposition of precursors ($Zn(CH_3COO)_2{\cdot}2H_2O$) + NH_4VO_3) in the absence (a) and presence (b, c) varying amounts of sucrose and the formation of (a) O_V-ZnV_2O_4-0, (b) O_V-ZnV_2O_4-100, and (c) O_V-ZnV_2O_4-200.

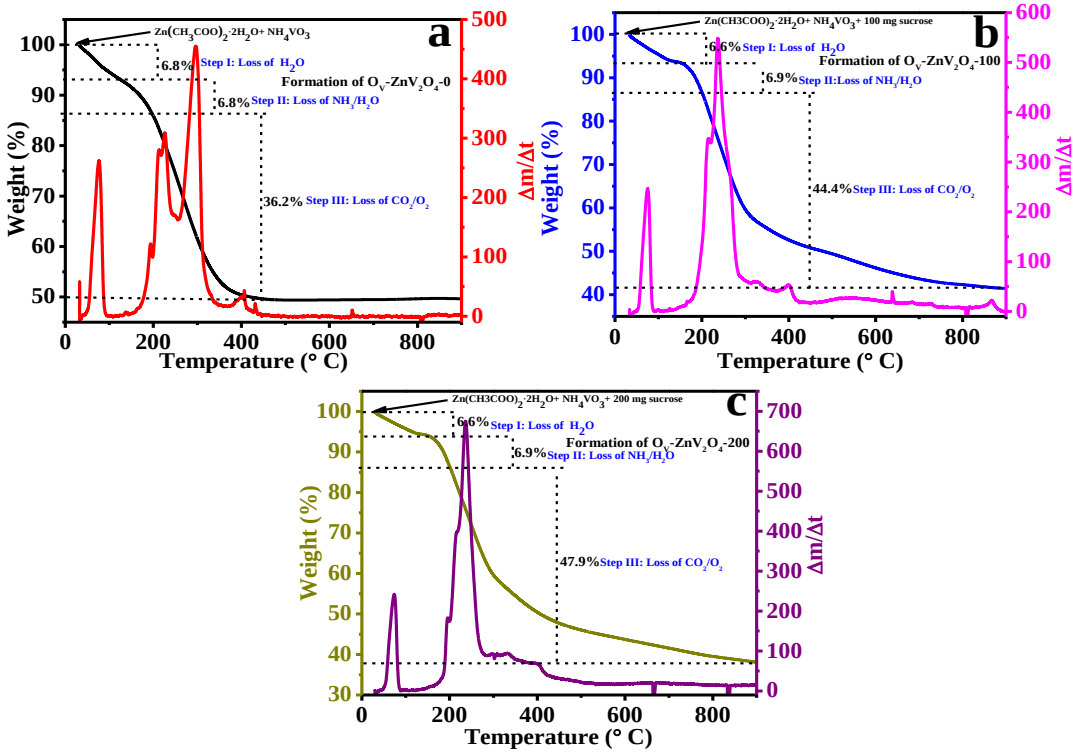

TG analyses were performed with the mixture of the precursors ($Zn(CH_3COO)_2{\cdot}2H_2O$) + NH_4VO_3) in the presence of varying amounts of sucrose (0, 100, and 200 mg). Multi-step weight loss was observed in all cases. In the absence of sucrose, three distinct weight losses were observed (Fig. S2a). The second and third weight losses (200-350°C) overlap when sucrose is present. The initial weight loss in step I (<130°C) is attributed to the loss of H_2O from $Zn(CH_3COO)_2{\cdot}2H_2O$ (Fig. S2a, b and c). Step II (>130°C) corresponds to the loss of NH_3 and structural H_2O due to the decomposition of NH_4VO_3.[1,2] The third weight loss can be attributed to the evolution of CO_2/O_2 and the final stable weight plateau observed above 450°C corresponds to the formation of carbon-supported ZnV_2O_4 as the final product. In the presence of sucrose, the well-defined plateau was not observed at the final stage possibly due to the presence of sucrose-derived carbon. The weight loss above 350°C in the presence of sucrose is associated with further loss of O_2. The quantitative analysis of the weight loss at various steps confirms that the final product has carbon and O_V-ZnV_2O_4. The % carbon content in the presence of sucrose is quantified to be 19.6% and 34.7% for the sample mixture analyzed in the presence of 100 and 200 mg of sucrose, respectively.

Fig. S3 EPR spectral profile of O_V-ZnV_2O_4-0, O_V-ZnV_2O_4-100, and O_V-ZnV_2O_4-200 at room temperature.

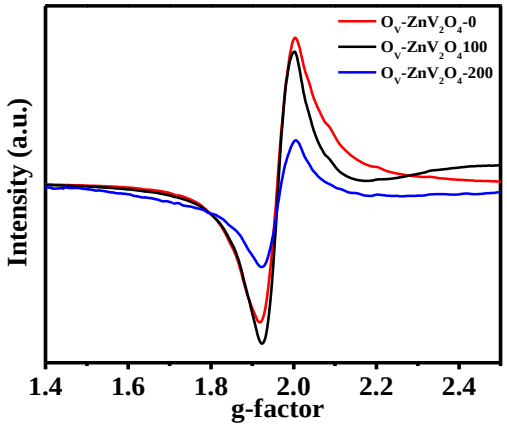

Fig. S4 (a) High-resolution XPS V 2p profile of O_V-ZnV_2O_4-0, O_V-ZnV_2O_4-100, and O_V-ZnV_2O_4-200. (b) The bar diagram depicts the % of different oxidation states of V.

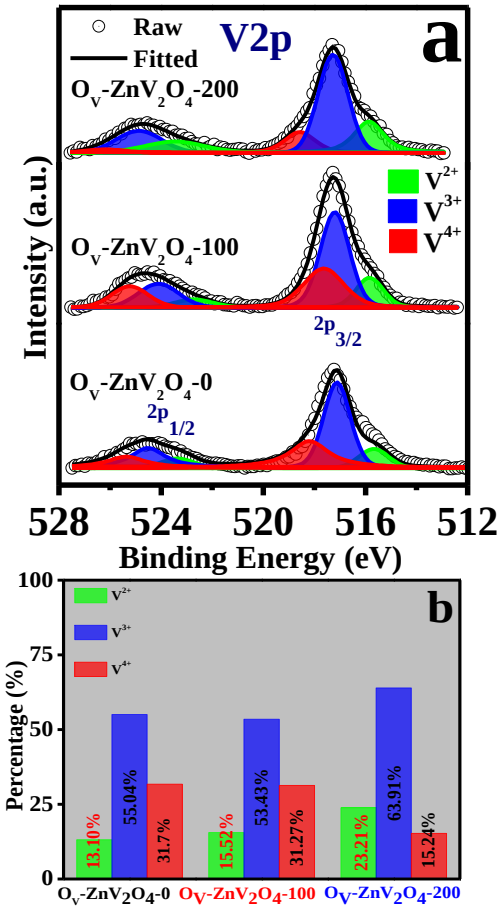

Fig. S5 High-resolution XPS O 1s profile of O_V-ZnV_2O_4-0 (a), O_V-ZnV_2O_4-100 (b), and (c) O_V-ZnV_2O_4-200.

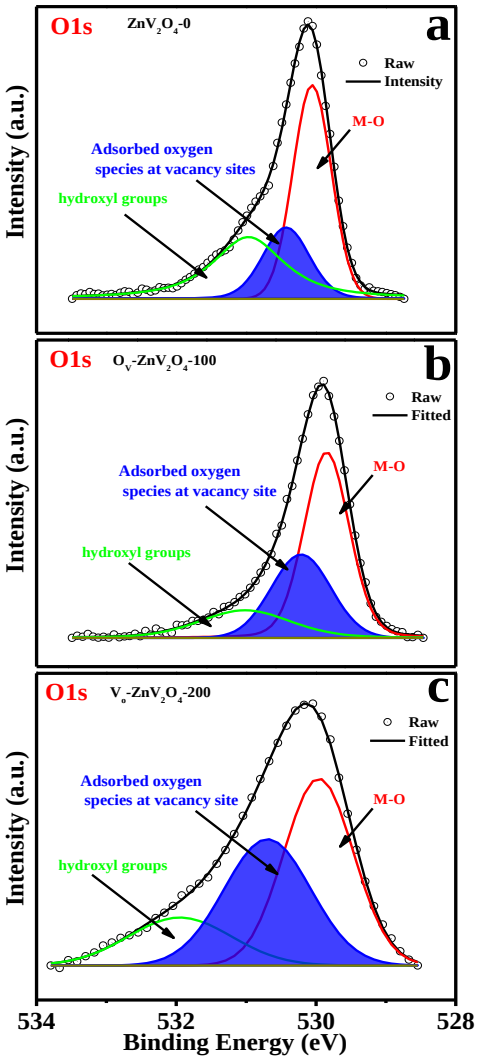

Fig. S6 FESEM images of O_V-ZnV_2O_4-0 (a), O_V-ZnV_2O_4-100 (b), and (c) O_V-ZnV_2O_4-200.

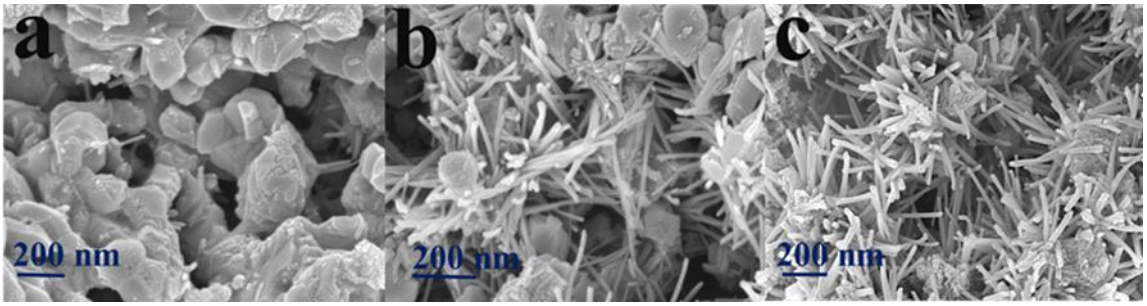

Fig. S7 HADDF image of O_V-ZnV_2O_4-200 and the corresponding STEM elemental mapping image illustrating the distribution of carbon.

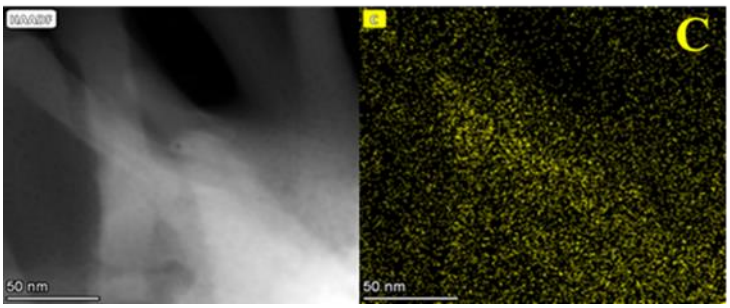

Fig. S8 (a) Galvanostatic charge-discharge profiles obtained for Zn||O_V-ZnV_2O_4-200 ZIB at 100 mA g^{-1} and (b) Comparison of first charge profile at the current density of 100 and 500 mA g^{-1}.

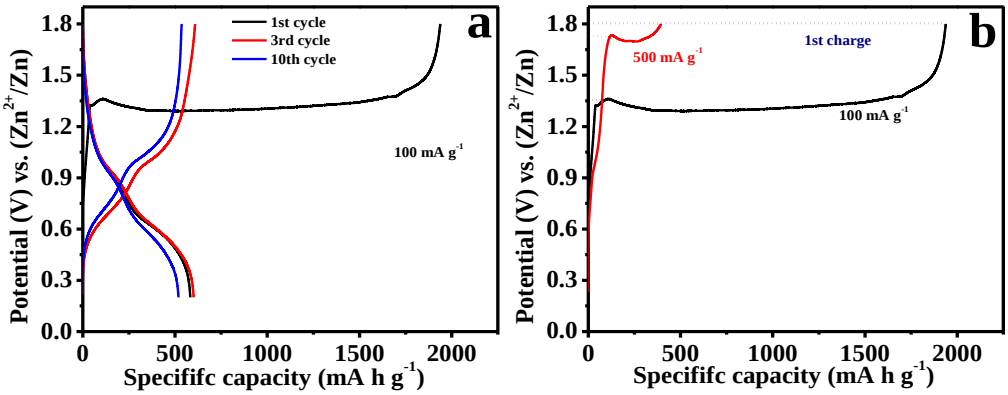

As shown in the figures, the potential-induced transformation of the cathode began at ~1.32 V at the low current density of 100 mA g^{-1} in contrast to 1.52 V at 500 mA g^{-1} (Fig. 3b). The conversion/transformation took a longer time at the lower current density. The cathode delivers a maximum capacity of 374.5 mAh g^{-1} (at 500 mA g^{-1}) after 10 charge-discharge cycles at a current density of 500 mA g^{-1}, whereas a maximum capacity of 600.1 mAh g^{-1} (100 mA g^{-1}) after 3 charge-discharge cycles at 100 mA g^{-1} was achieved. It is worth pointing out here that the specific capacity at a particular current density after activation remains the same irrespective of the current density (low or high) at which the cathode is activated.

Fig. S9 (a) Galvanostatic charge-discharge profile of Zn||O_V-ZnV_2O_4-200 ZIB at different current densities. Plot illustrating the cycling stability of O_V-ZnV_2O_4-200 at the current densities of (b) 100 mA g^{-1} and (c) 2000 mA g^{-1}.

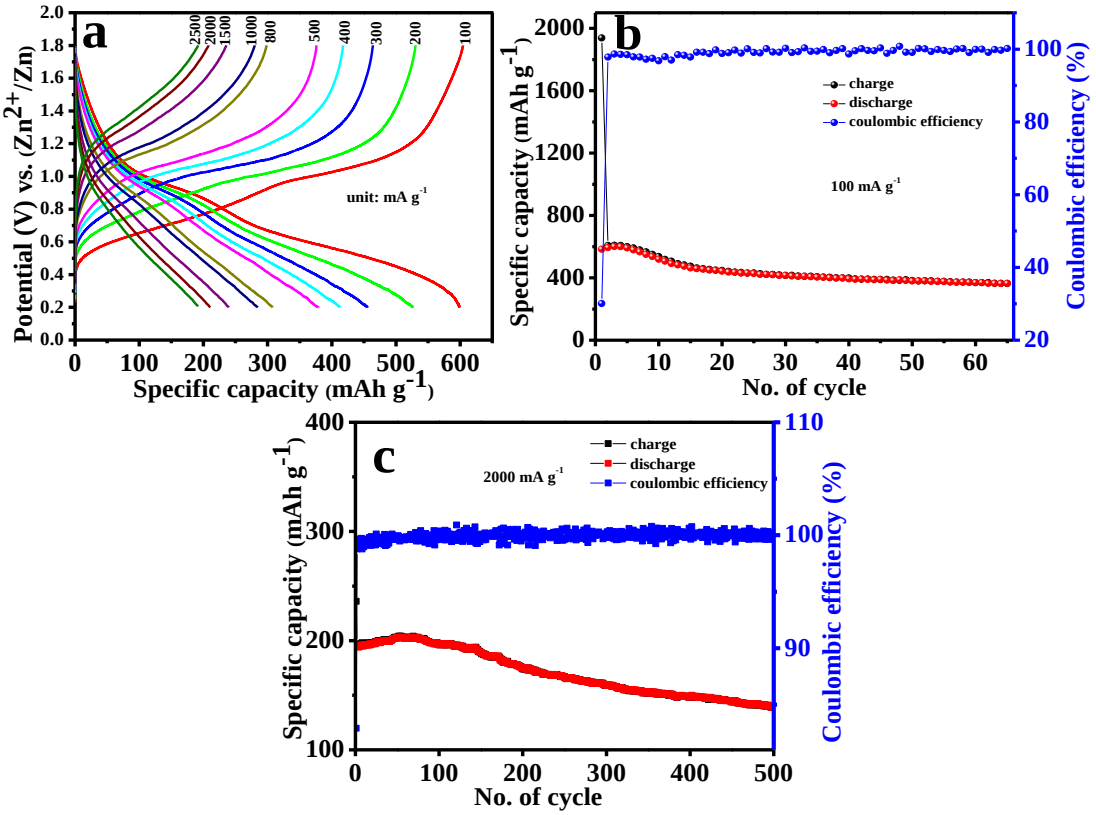

Fig. S10 Galvanostatic charge-discharge profile (a) and plot illustrating the cycling stability of O_V-ZnV_2O_4-0, O_V-ZnV_2O_4-100, and O_V-ZnV_2O_4-200 at 500 mAg^{-1} (b). (c) Nyquist plots at open circuit voltage and a table summarizing the charge transfer resistance.

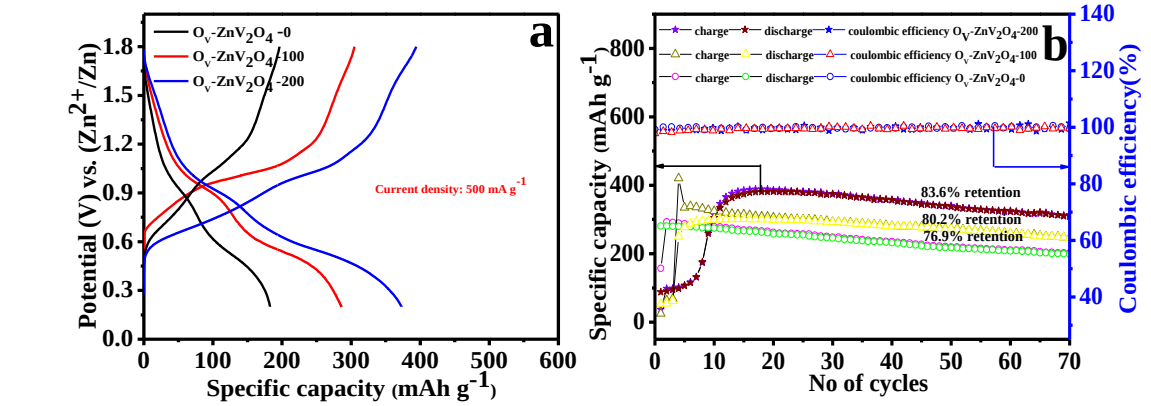

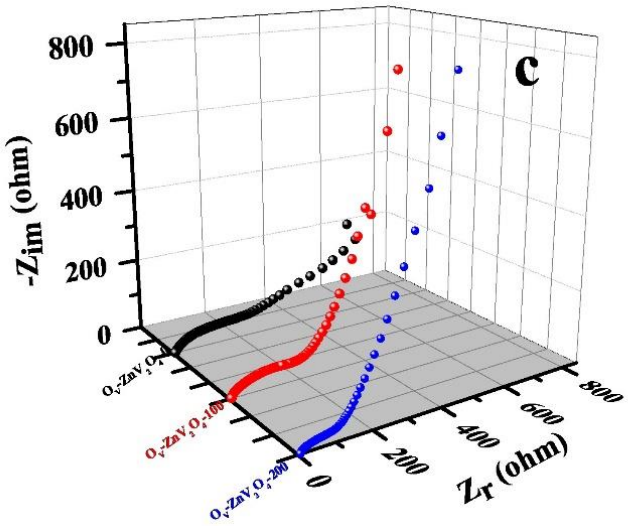

Cathode	R_{ct} (ohm)
O_V-ZnV_2O_4-0	260.8
O_V-ZnV_2O_4-100	214.3
O_V-ZnV_2O_4-200	180.1

Note S1: Analysis of Galvanostatic Intermittent Titration Technique (GITT) study

$$D = \frac{4}{\pi\tau}\left(\frac{n_m V_m}{S}\right)^2\left(\frac{\Delta E_s}{\Delta E_t}\right)^2 \qquad (1)^{3,4}$$

D is the diffusion coefficient, n_m, and V_m are the number of moles of the active material and the molar volume, respectively, and S is the contact area between the electrode and electrolyte. t is the time duration of the pulse. ΔE_s and ΔE_t are the quasi-equilibrium and battery voltage changes, respectively.

Fig. S11 GITT profile of a single step during the discharge of Zn||O_V-ZnV_2O_4-200.

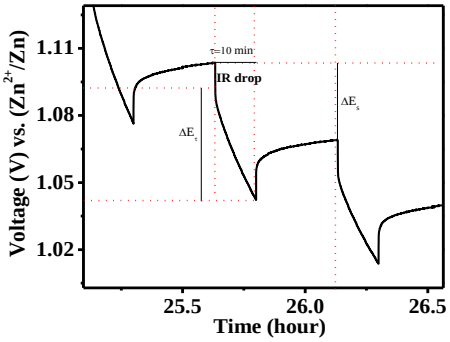

Fig. S12 Plots illustrating the diffusion coefficient vs ion insertion state for O_V-ZnV_2O_4-0 (a), and O_V-ZnV_2O_4-100 (b).

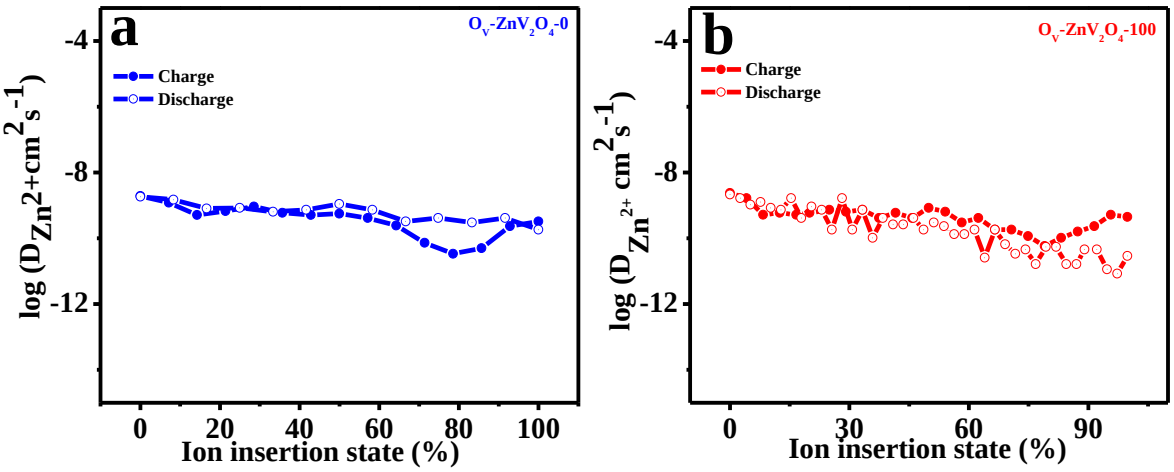

Fig. S13 Nyquist plot at OCV (1.1 V) and after different cycles in charge state at 1.8 V (O_V-ZnV_2O_4-200 cathode). Table summarizing the charge transfer resistance. The equivalent circuit is shown in the inset: R_s: solution resistance, R_{ct}: charge transfer resistance, CPE: constant phase element, and W: Warburg impedance.

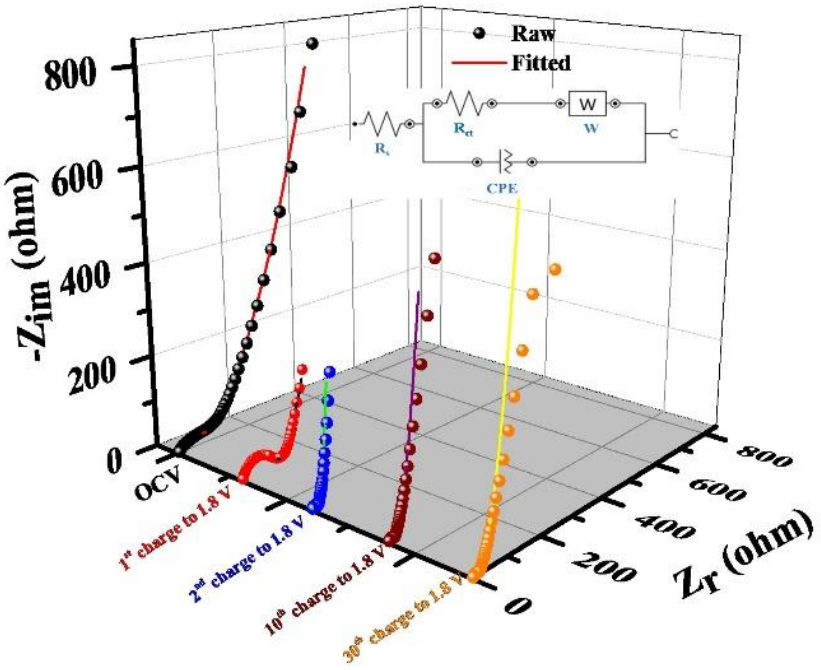

State	R_{ct} (ohm)
OCV	180.1
1st charge to 1.8 V	94.2
2nd charge to 1.8 V	14.1
10th charge to 1.8 V	12.4
30th charge to 1.8 V	12.1

Fig. S14 Nyquist plot at OCV (1.1 V) and after different cycles in discharge state at 0.2 V (O_V-ZnV_2O_4-200 cathode). Table summarising the charge transfer resistance.

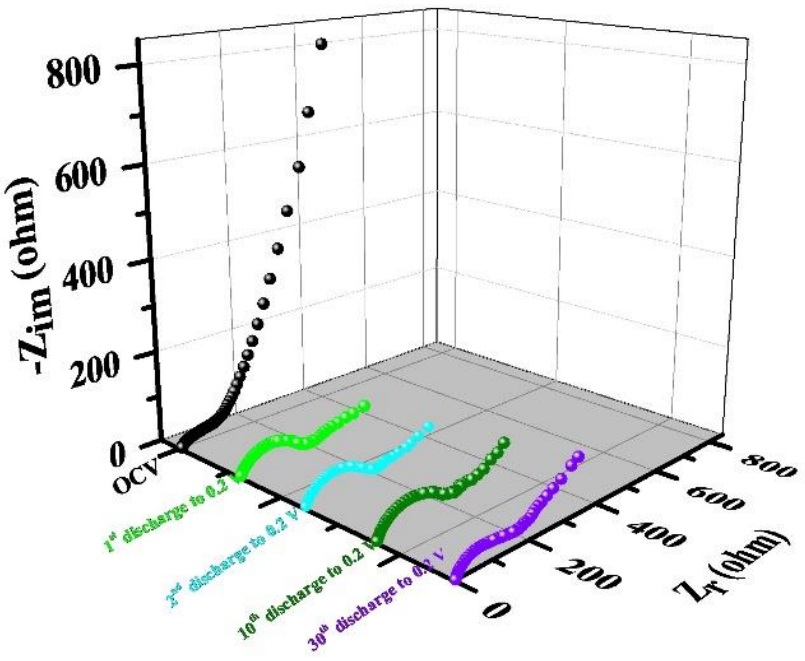

State	R_{ct} (ohm)
OCV	180.1
1st discharge to 0.2 V	192.1
2nd discharge to 0.2 V	196.2
10th discharge to 0.2 V	229.5
30th discharge to 0.2 V	205.8

Fig. S15 The calculated partial density of states (PDOS) of O_v-ZnV_2O_4.

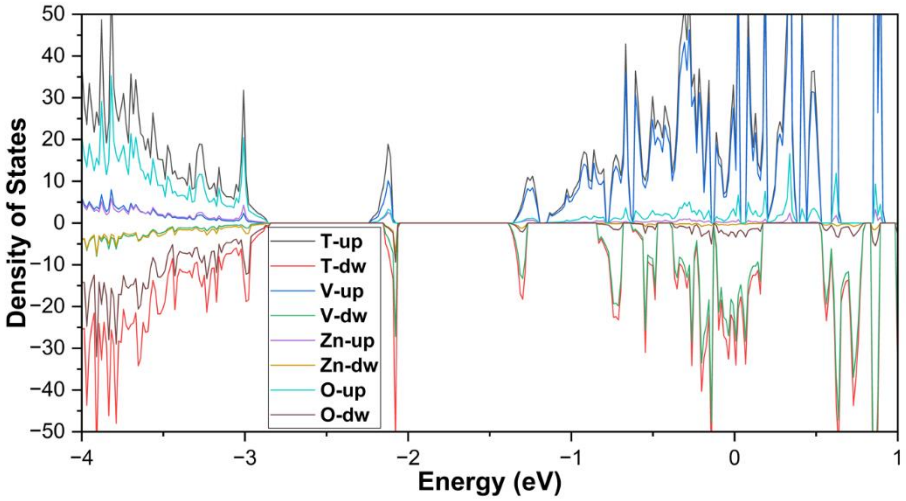

Fig. S16 Zn^{2+} ion interaction with (a) pristine ZnV_2O_4, and (b) O_V-ZnV_2O_4, and the calculated values of interaction energy. [Color code: grey sphere for Zn, red (big) sphere for V, and red (small) sphere for O].

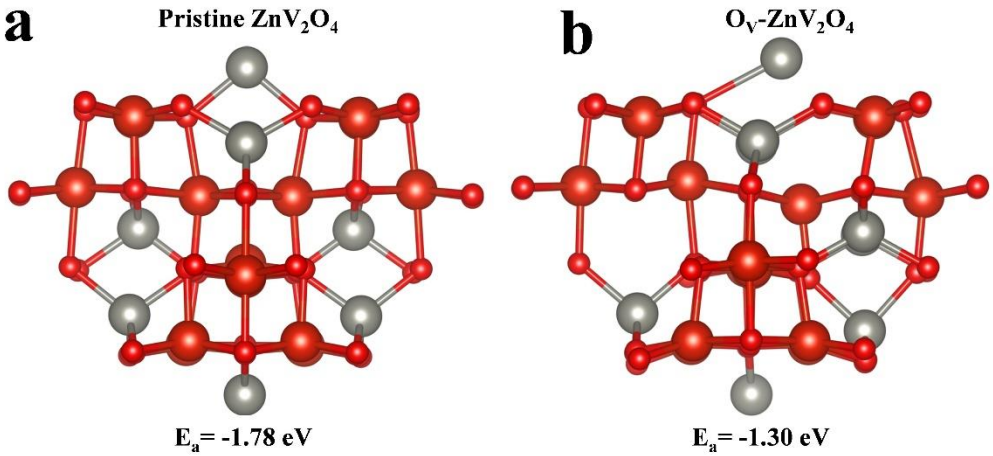

Note S2. Limitations of our calculation:

Our current level of theory (PBE-GGA) has limitations in accurately describing the electronic structure of systems containing transition metals, lanthanides, and actinides. To address these limitations, we recommend using advanced approaches incorporating U+V corrections. Standard DFT, particularly with local or semi-local exchange-correlation functionals like LDA or GGA, often fails to accurately describe systems with strong electron-electron correlations, such as transition metal oxides, lanthanides, and actinides. U+V corrections help account for these strong correlations by introducing on-site (U) and inter-site (V) Coulomb interactions. The Hubbard U term corrects the self-interaction error in DFT, better describing the localized d or f electrons in transition metals and rare earth elements. It effectively increases the energy gap and corrects the electronic structure by accounting for electron-electron repulsion within the same atomic site. The inter-site V term extends the correction to include interactions between electrons on different sites, crucial for materials where electron correlation effects involve neighboring atoms or ions.

By including U+V corrections, DFT can more accurately predict electronic properties such as band gaps, magnetic moments, and charge transfer insulators, often underestimated by standard DFT methods.

Fig. S17 Cyclic voltammograms of O_V-ZnV_2O_4-0, O_V-ZnV_2O_4-100, and O_V-ZnV_2O_4-200.

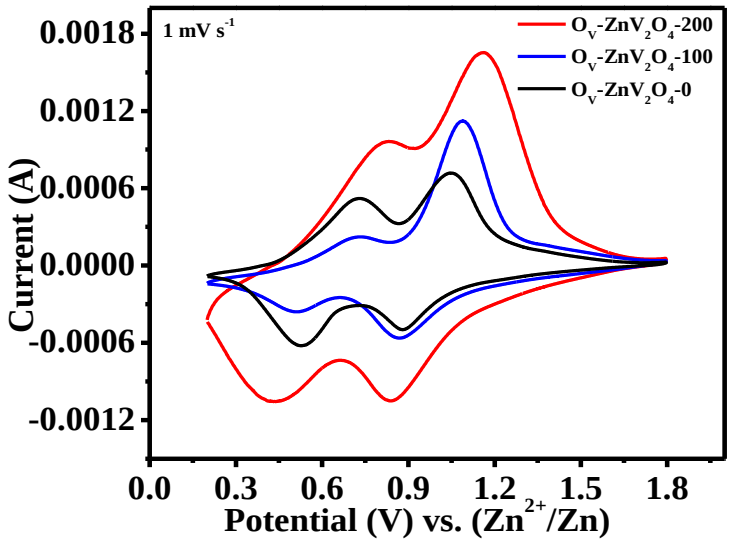

Note S3: Determining the capacitive and diffusion-controlled contributions:

The voltammogram was quantitatively analysed to understand the Zn^{2+} storage kinetics according to the eqn (1).[5]

$$i = a\nu^{b} \qquad (1)$$

where, 'a' and 'b' are the adjustable parameters and the value of b ranges from 0.5 to 1.0. The b-value is obtained from log(*i*)-log (ν) plots and the value of 'b' for the four peaks A, B, C and D are calculated to be 0.63, 0.69, 0.71 and 0.67, respectively, suggesting a diffusion-dominated process. The capacitive contribution is further calculated according to the following eqn (2)

$$i = k_1 + k_2\nu^{1/2} \qquad (2)$$

where, i refers to current (mA), the k_1 and k_2 are two potential dependent constant and v the scan rate mV s^{-1}. The k_1 and k_2 were calculated by plotting i vs. $v^{1/2}$ and k_1v and $k_2v^{1/2}$ correspond to the contribution from the capacitive and diffusion control process, respectively.

Fig. S18 Cyclic voltammograms at different scan rates (a), plot illustrating b-value and log (*i*)-log (ν) plot (b), cyclic voltammogram illustrating the capacitive contribution at the scan rate of 1 mV s^{-1} (c), and plot illustrating the capacitive and diffusion-controlled contribution at various scan rate (d).

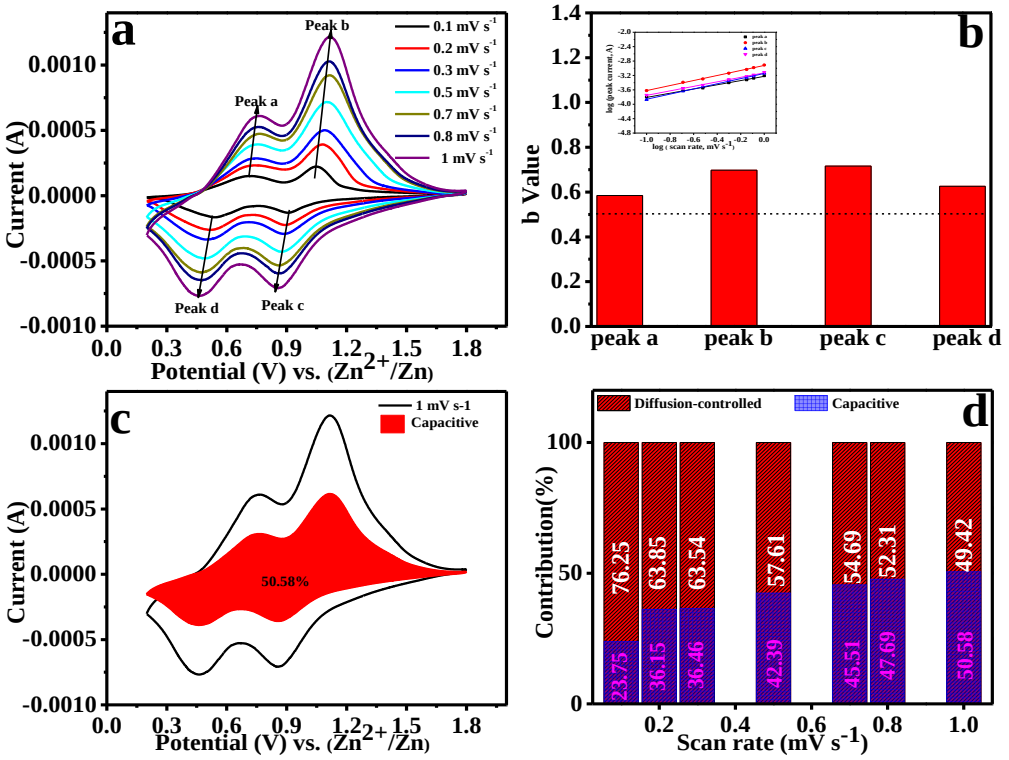

Fig. S19 Capacitive and diffusion-controlled current contribution at 1 mV s^{-1} of O_V-ZnV_2O_4-0, O_V-ZnV_2O_4-100, and O_V-ZnV_2O_4-200.

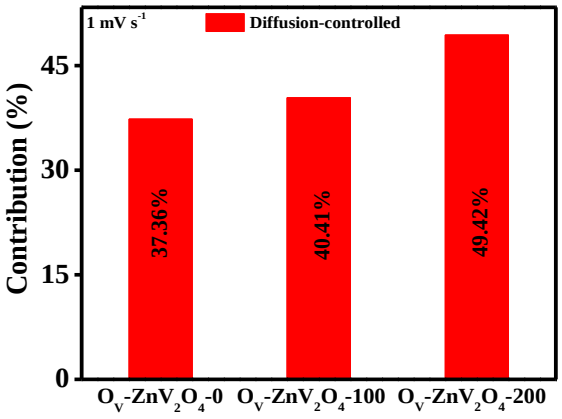

Fig. S20 (a) High-resolution ex-situ XPS V 2p profile of O_V-ZnV_2O_4-200 at different charge and discharge states. (b) The bar chart represents the % of different oxidation states of V at different states of charge-discharge.

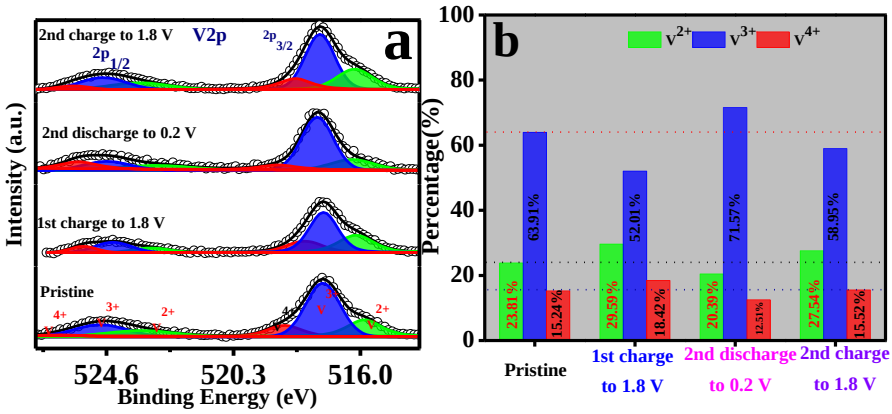

Fig. S21 (a) Cyclic voltammograms (first three cycles) of Zn||O_V-ZnV_2O_4-200 at 3 mV s^{-1}, and (b) galvanostatic charge-discharge profiles at 500 mA g^{-1}. Electrolyte: Zn $(CF_3SO_3)_2$ in dry acetonitrile.

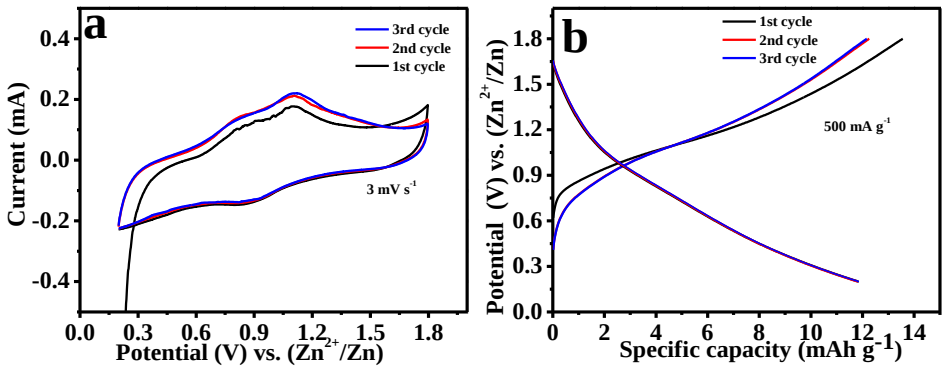

Fig. S22 FESEM (a, d), TEM (b, e), and HRTEM (c, f) images of O_V-ZnV_2O_4-200 cathode when charged to 1.8 V (a-c) and discharged to 0.2 V (d-g). STEM elemental mapping (Zn, V, O, C, S, and F) of the cathode at the discharge state (0.2 V). The inverse FFT image is shown in the inset of (f).

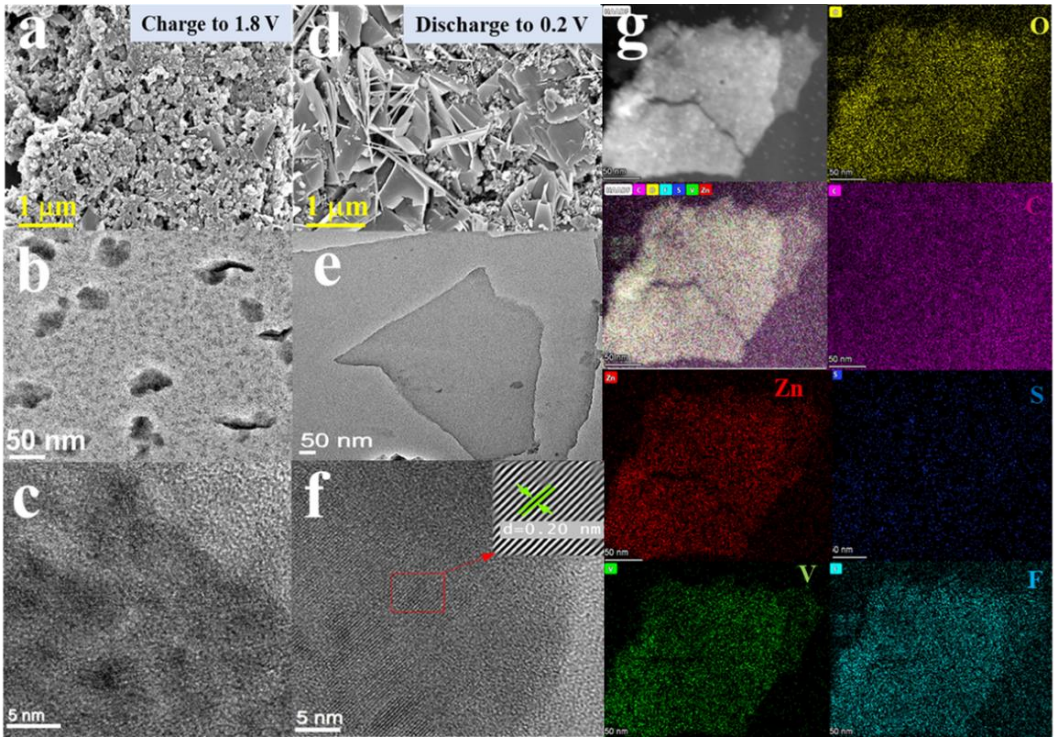

Fig. S23 High-resolution XPS C1s profile of O_V-ZnV_2O_4-200 cathode at pristine, fully charged, and discharged states.

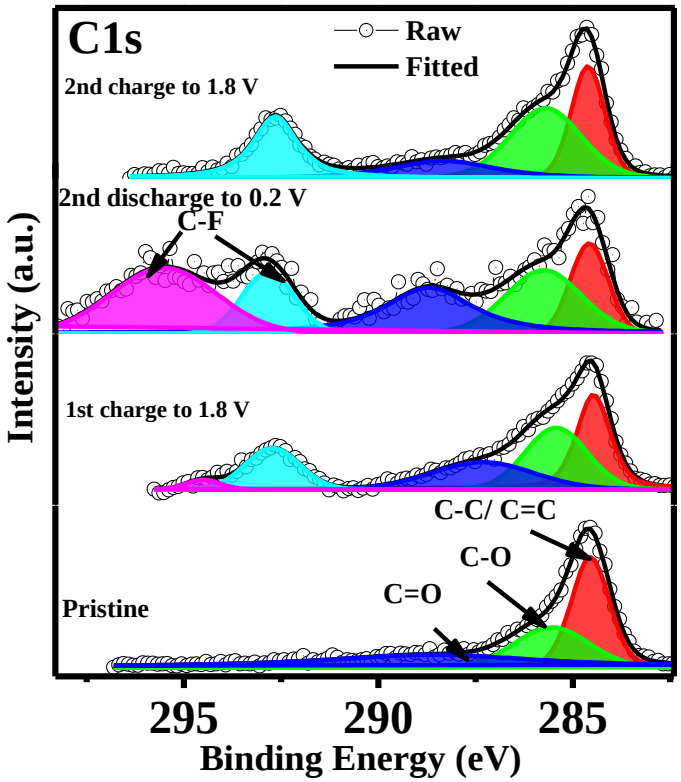

Fig. S24 Schematic illustration of the charge-storage with O_V-ZnV_2O_4-200.

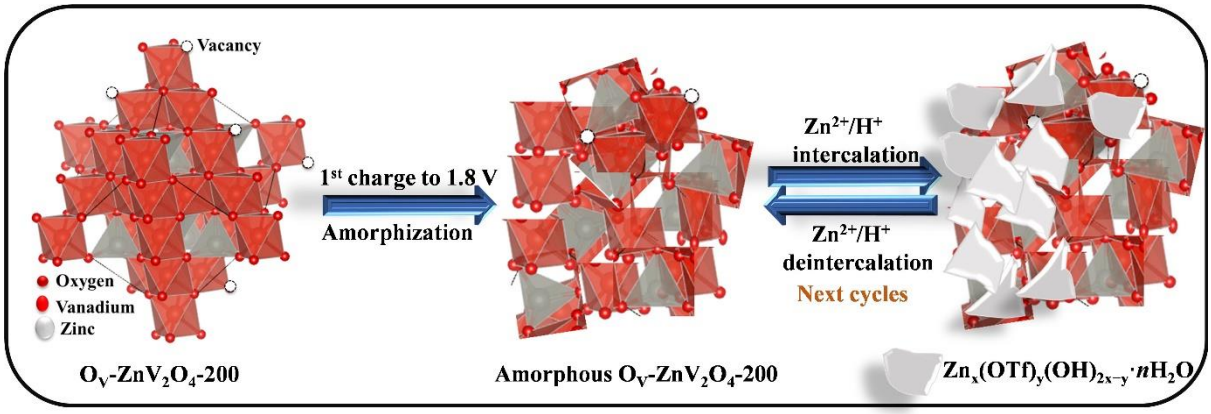

Fig. S25 Digital photograph of OCV of a single coin cell and ZIB-powered LCD panel of digital hygrometer.

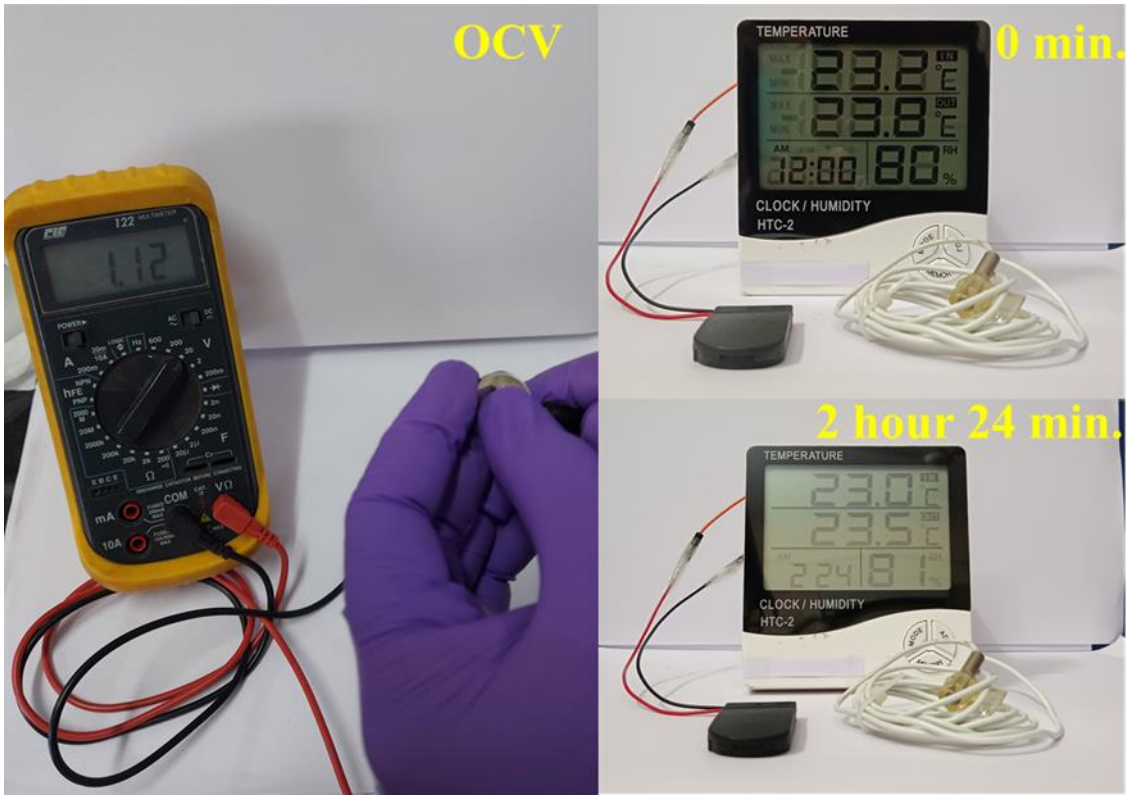

Table S1. ZIB performance of low valent vanadium-based spinel cathode.

Sl No.	Cathode Material	Electrolyte	Reaction mechanism	Voltage (V) vs. Zn^{2+}/Zn	Specific capacity	Energy density Wh kg^{-1}	Power density W kg^{-1}	Capacity retention / cycles/ current density	Ref
1	Electroactivation-induced spinel ZnV_2O_4	2M $Zn(ClO_4)_2$		0.2–1.4	312 mAh g^{-1} at 0.5 C			84%/ 1000/ 10 C	6
2	ZnO/ZnV_2O_4 composite hollow microspheres	3 M $Zn(CF_3SO_3)_2$		0.2–1.8	338 mAh g^{-1} at 100 mA g^{-1}	260.8	76.9	79%/ 2000/ 4000 mA g^{-1}	7
3	Porous structure ZnV_2O_4/C-N composite	2 M $ZnSO_4$		0.5–1.8	301 mAh g^{-1} at 300 mA g^{-1}			/ 1000/ 200 mA g^{-1}	8
4	Act−ZnV_2O_4	3 M $ZnSO_4$	Insertion/extraction of Zn^{2+}	0.4–1.6	242 mAh g^{-1} at 500 mA g^{-1}			83%/ 2000/ 4000 mA g^{-1}	9
5	Urchin-like Spinel MgV_2O_4	2M $Zn((CF_3SO_2)_2N)_2$	Insertion/extraction of Zn^{2+}	0.2-1.4	272 mAh g^{-1} at 200 mA g^{-1}	171.5	140.6		10
6	Sea-urchin-like oxygen–deficient ZnV_2O_4	3 M $Zn(CF_3SO_3)_2$	Co-insertion/extraction of Zn^{2+} and H^+	0.2-1.8	599.6mAh g^{-1} at 100 mA g^{-1}	371.8	62.1	57.5%/2300/4000	**this work**

References:

[1] Y. Li, S. Zhang, S. Wang, Z. Xiao, F. Meng, Q. Li, X. Zhang, Z. Zhang, L. Zhi, and Z. Tang, *Adv. Energy Mater.*, 2023, **13**, 2203810.

[2] T. Wanjun, L. Yuwen, Y. Xi, and W. Cunxin, *Ind. Eng. Chem. Res*., 2004, **43**, 2054.

[3] Y. Zhu, T. Gao, X. Fan, F. Han and C. Wang, *Acc. Chem. Res.*, 2017, **50**, 1022–1031.

[4] F. Ming, H. Liang, Y. Lei, S. Kandambeth, M. Eddaoudi and H. N. Alshareef, *ACS Energy Lett.*, 2018, **3**, 2602–2609.

[5] J. Wang, J. Polleux, J. Lim and B. Dunn, *J. Phys. Chem. C*, 2007, **111**, 14925–14931.

[6] Y. Liu, C. Li, J. Xu, M. Ou, C. Fang, S. Sun, Y. Qiu, J. Peng, G. Lu, Q. Li, J. Han and Y. Huang, *Nano Energy*, 2020, **67**, 104211.

[7] P. Luo, W. Tang, W. Cai, J. Yang, C. Zuo, G. Liu, Y. Xiao and S. Dong, *J. Solid State Chem.*, 2021, **301**, 122371.

[8] S. Li, L. Qin, L. Li, H. Cheng, G. Fang, S. Liang, Q. Zhu and M. Chen, *Mat. Today Commun.*, 2021, **27**, 102271.

[9] T. Wu, K. Ni, B. Liu and S.-H. Wang, *ACS Appl. Energy Mater.*, 2022, **5**, 10196–10206.

[10] W. Tang, B. Lan, C. Tang, Q. An, L. Chen, W.-W. Zhang, C. Zuo, and S. Dong, *ACS Sustainable Chem. Eng.*, 2020, **8**, 3681−3688.